

Article

Mechanical Properties and Microstructure Evolution of Mg-Gd Alloy during Aging Treatment

Yi Liu ¹, Yang Song ¹, Na Li ¹, Xuechao Sha ², Mengning Xu ¹, Bin Chen ³, Bo Gao ¹, Lirong Xiao ^{1,*} 
and Hao Zhou ^{1,*}

¹ Nano and Heterogeneous Materials Center, School of Materials Science and Engineering, Nanjing University of Science and Technology, Nanjing 210094, China; liuyi9280@njust.edu.cn (Y.L.); 9211160d0532@njust.edu.cn (Y.S.); lina52566@njust.edu.cn (N.L.); sunnymxn@163.com (M.X.); gaobo@njust.edu.cn (B.G.)

² Beijing Key Lab of Microstructure and Property of Advanced Materials, Beijing University of Technology, Beijing 100124, China; xuechao.sha@zeiss.com

³ ThermoFisher Scientific, Shanghai, Shanghai 201210, China; bin.chen@thermofisher.com

* Correspondence: xiaolr620@126.com (L.X.); hzhou511@njust.edu.cn (H.Z.)

Abstract: Rare-earth-containing Mg alloys are a group of widely investigated alloys due to the disperse nano-sized precipitations formed during heat treatment. The underlying formation and strengthening mechanisms of precipitation is critical for their industrial applications. In this work, we systematically studied the evolution of precipitations in a Mg-10Gd alloy, based on the atomic-scaled TEM and HAADF-STEM observations. Especially, the in-depth transition mechanism from G.P. Zone to β'' , β' , β_T and β_M is proposed, as well as their relationships with mechanical properties. It is found that blocking effect of precipitations improves the strength significantly, according to the Orowan mechanism. The elliptic cylinder shaped β' phase, with a base-centered orthorhombic lattice structure, provides significant strengthening effects, which enhance the hardness and ultimate tensile strength from 72 HV and 170 MPa to 120 HV and 300 MPa.



Citation: Liu, Y.; Song, Y.; Li, N.; Sha, X.; Xu, M.; Chen, B.; Gao, B.; Xiao, L.; Zhou, H. Mechanical Properties and Microstructure Evolution of Mg-Gd Alloy during Aging Treatment. *Metals* **2022**, *12*, 39. <https://doi.org/10.3390/met12010039>

Academic Editor: Alberto Moreira Jorge Junior

Received: 18 November 2021

Accepted: 22 December 2021

Published: 24 December 2021

Publisher's Note: MDPI stays neutral with regard to jurisdictional claims in published maps and institutional affiliations.



Copyright: © 2021 by the authors. Licensee MDPI, Basel, Switzerland. This article is an open access article distributed under the terms and conditions of the Creative Commons Attribution (CC BY) license (<https://creativecommons.org/licenses/by/4.0/>).

Keywords: Mg-Gd alloy; precipitation; mechanical properties; HAADF-STEM

1. Introduction

As the lightest structural metal in industrial applications, magnesium alloys have been intensively investigated due to their contributions in energy conservation and environment protection [1–4]. Owing to their hexagonal close-packed (HCP) lattice structure, the easy slip systems in Mg alloys are insufficient to support the stable plastic deformation at room temperature [5–10]. It is well established that the factor of Hall–Petch equation of Mg alloys is high, while the strengthening is difficult to achieve by work hardening, because of the low ductility [11–17]. Recent research has revealed that precipitation hardening is the most effective way to improve the strength of Mg alloys at both room temperature and elevated temperatures [18–22].

Compared with conventional wrought Mg alloys, including Mg-Sn, Mg-Al and Mg-Zn system alloys, the Mg alloys containing rare earth elements exhibit outstanding strengthening effects, such as the solution strengthening and age hardening [23–26]. Gadolinium (Gd) is one of the most popular rare earth elements in Mg alloys, because its solubility decreases rapidly with the decreasing of temperature [27]. Aging treatment is an effective way to enhance the strength of Mg-Gd system alloys, owing to the disperse nano-sized precipitations. High density of precipitations with nano size are formed to provide blocking effect on dislocation, thus improving the mechanical properties significantly [28–30]. In general, the effect of age hardening is affected by many factors, such as temperature, time, content and type of elements [31–35]. The structures of precipitations in Mg-Gd system alloys have a specific evolution sequence, which is proposed as: S.S.S.S (Supersaturated Solid solution) $\beta'' \rightarrow \beta_T \rightarrow \beta' \rightarrow \beta_1 \rightarrow \beta$ [24]. Li et al. produced a Mg-14Gd alloy with high

tensile strength of 445 MPa after aging treatment, in which the significant enhancement of strength is contributed by the cylindrical precipitate β' phase [36]. He et al. reported that β' phase has a base-centered orthorhombic (b.c.o.) structure with lattice parameters of $a = 0.64$ nm, $b = 2.22$ nm, $c = 0.52$ nm, which was identified by electron microdiffraction analysis [37]. Nie et al. reported that β' phase has a stoichiometry of Mg_7Gd with lattice parameters of $a = 0.650$ nm, $b = 2.272$ nm, and $c = 0.521$ nm [38]. It has been revealed that the cylindrical precipitates provide highest blocking effect, thus increasing the critical shear stress (CRSS) of dislocation slips [39].

Given that the β' phase is the main strengthening precipitate in Mg-Gd alloy, it is therefore critical to fully understand its formation and strengthening mechanism. In the present work, the evolution of precipitations and their corresponding effect on the mechanical properties of a Mg-10Gd alloy are systematically investigated using atomic-scaled transmission electron microscope (TEM) and high-angle annular dark-field scanning transmission electron microscope (HAADF-STEM) characterizations. The relationship between microstructures and mechanical properties during aging treatment is bridged.

2. Materials and Methods

The Mg-10Gd (wt.%) alloy used in this study were prepared from high-purity Mg and Gd (99.95%) using an electric-resistant furnace protected by a mixed atmosphere of CO_2 and SF_6 . The as-cast ingots were solution treated at 520 °C for 8 h, followed by quenching in warm water with 70 °C. Isothermal aging were performed at 200 °C, 225 °C and 250 °C for 0–250 h, respectively. The microstructural evolution of Mg-10Gd alloy treated at 200 °C for 0–250 h were observed by optical microscopy (OM) (BX41, OLYMPUS, Tokyo, Japan), all samples were ground with sandpaper of 320, 800, 1200 and 2000 grits, then polished by a woolen cloth with 1 μ m diamond suspension to a mirror finish surface. The etching solution was comprised of 50 mL ethyl alcohol with 3 g picric acid, 20 mL deionized water and 20 mL acetic acid, and the holding time for etching is about 10–15 s. The average grain sizes were calculated by the linear intercept method for measuring \sim 100 grains.

The Vickers hardness were tested by a HVM-G hardness tester (Shimadzu, Kyoto, Japan) with a load of 150 g and a holding time of 15 s. At least 10 indents for each sample were recorded to ensure the accuracy of the results. The samples for tensile test were cut into dog-bone-shaped specimens, with gage length, width and thickness of 8 mm, 6.6 mm and 1.5 mm, respectively. Quasi-static uniaxial tensile tests were performed on a LTM-20KN testing machine (walter+bai ag, Löhningen, Switzerland) with a strain rate of $3 \times 10^{-3} s^{-1}$. The TEM specimens were polished using SiC abrasive papers of 320-2000# to a thickness of \sim 60 μ m. Then, the pre-thinning process was performed using a Dimple Grinder machine (Gatan Model 657) (Gatan, Pleasanton, CA, USA) to further reduce the thickness to \sim 25 μ m. Ion milling was carried out using Precision Ion Polishing System (PIPS, Gatan model 695) (Gatan, Pleasanton, CA, USA) at -25 °C with low angle ($<3.5^\circ$) with an ion beam energy of 3 KeV. Atomic-resolution high-angle annular dark-field (HAADF) observation was carried out on an aberration-corrected scanning transmission electron microscope (STEM) (Titan G2 60-300) (Thermofisher, Hillsboro, OR, USA) with accelerate voltage of 300 kV. The atomic model was established using CrystalMaker software (Version2.5.1, CrystalMaker® for Windows, UK).

3. Results and Discussion

Figure 1a shows the aging hardening curves of Mg-10Gd alloy treated at different temperatures. The initial micro-hardness is \sim 72 HV. In this stage, solid solution is the main strengthening mechanism. Moreover, the stacking fault energy is significantly decreased by rare earth (Gd), which introduces non-basal slips to increase the ductility of Mg alloys [40]. The sample aged at 200 °C for 70 h exhibits a highest hardness of \sim 120 HV. Note that, the grain size keeps stable in a range of 130–150 μ m during the whole aging treatment (Figure 1b, more details are shown in optical view, marked by red dotted box). Thus, the improvement of hardness is mainly due to the precipitations.

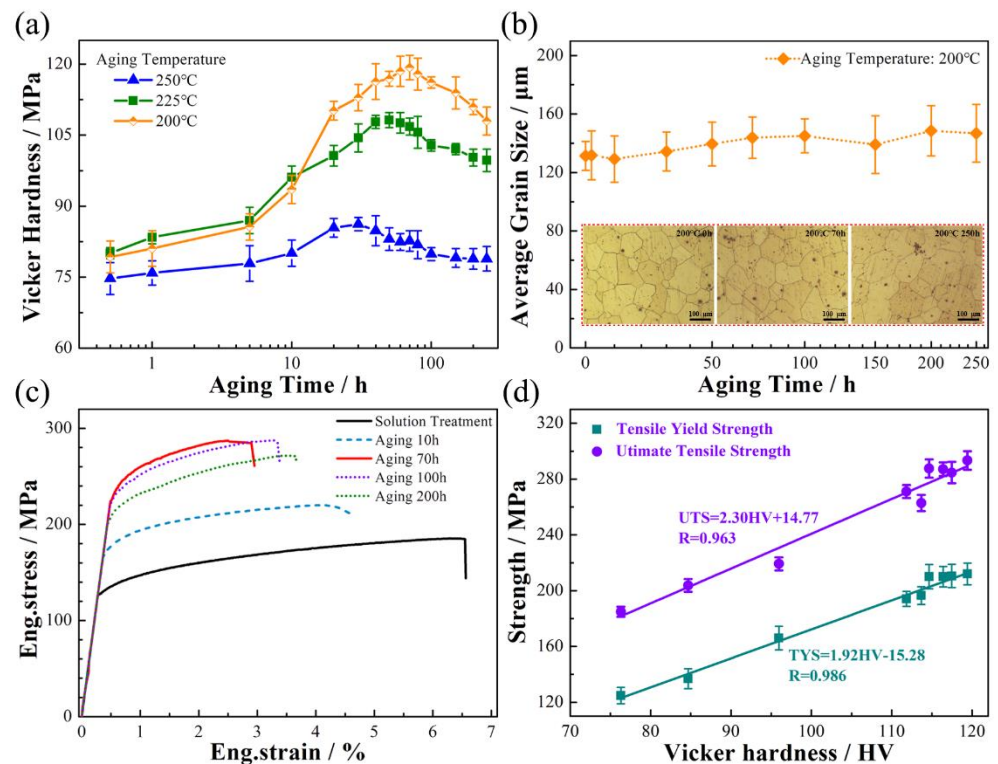


Figure 1. Mechanical properties of the aged Mg-10Gd alloys. (a) Vickers hardness curves of the samples aged at 200 °C, 225 °C and 250 °C, respectively; (b) a stable grain size during aging treatment at 200 °C, the inserted image as marked by red dotted box shows grain size with ageing time for 0 h, 70 h, 250 h, respectively; (c) engineering stress-strain curves of the samples aged at 200 °C with different times; (d) a high linear correlation between strength and hardness of the sample aged at 200 °C.

Figure 1c shows the tensile stress–strain curves of samples aged at 200 °C. Before aging treatment, the Tensile Yield Strength (TYS), Ultimate Tensile Strength (UTS) and uniform elongation were 125 MPa, 170 MPa and 6.4%, respectively. The strength shows a significant improvement with increasing of aging time. The peak aged condition occurred at 70 h, and the TYS and UTS enhanced to 250 MPa and 300 MPa, respectively. On another side, all the aged samples exhibited decrease of ductility. The uniform elongation of the peak aged sample is only 3%. Figure 1d shows the relationship between strength and hardness. The linear fitting equation can be approximated as:

$$\text{TYS} = 1.92 \text{ HV} - 15.28 \quad (1)$$

$$\text{UTS} = 2.3 \text{ HV} + 14.77 \quad (2)$$

The factor of R-Square of Equations (1) and (2) are 0.986 and 0.963, indicating a high linear correlation between strength and hardness. Thus, the improvement of strength can be simply predicted by the values of hardness.

The significant improvement of strength in Mg-10Gd alloy is due to the dissolution of Gd from the Mg matrix, forming high density of nano-scaled precipitations. Nucleation of precipitation starts at very early stage of aging treatment (0.5 h), as marked by the white arrows in Figure 2a,b. However, neither the bright field image in Figure 2a or the selected area diffraction pattern (SADP) in Figure 2b cannot obtain the exact microstructure of the precipitates clearly. Consequently, how to trace the position of Gd atom is critical to reveal the formation mechanism of the precipitations. According to Equation (3), the intensity of

atomic columns in a HAADF-STEM image is approximately proportional to the square of the atomic number Z [41].

$$\sigma_{(\theta)} = \frac{e^4 Z^2 d\Omega}{16(4\pi\epsilon_0 E_0)^2 \sin^4 \frac{\theta}{2}} \quad (3)$$

where σ is scattering cross section, θ is scattering semi-angle, Ω is solid angle, e is electron charge, Z is atomic number, ϵ_0 is dielectric constant and E_0 is energy of the electrons.

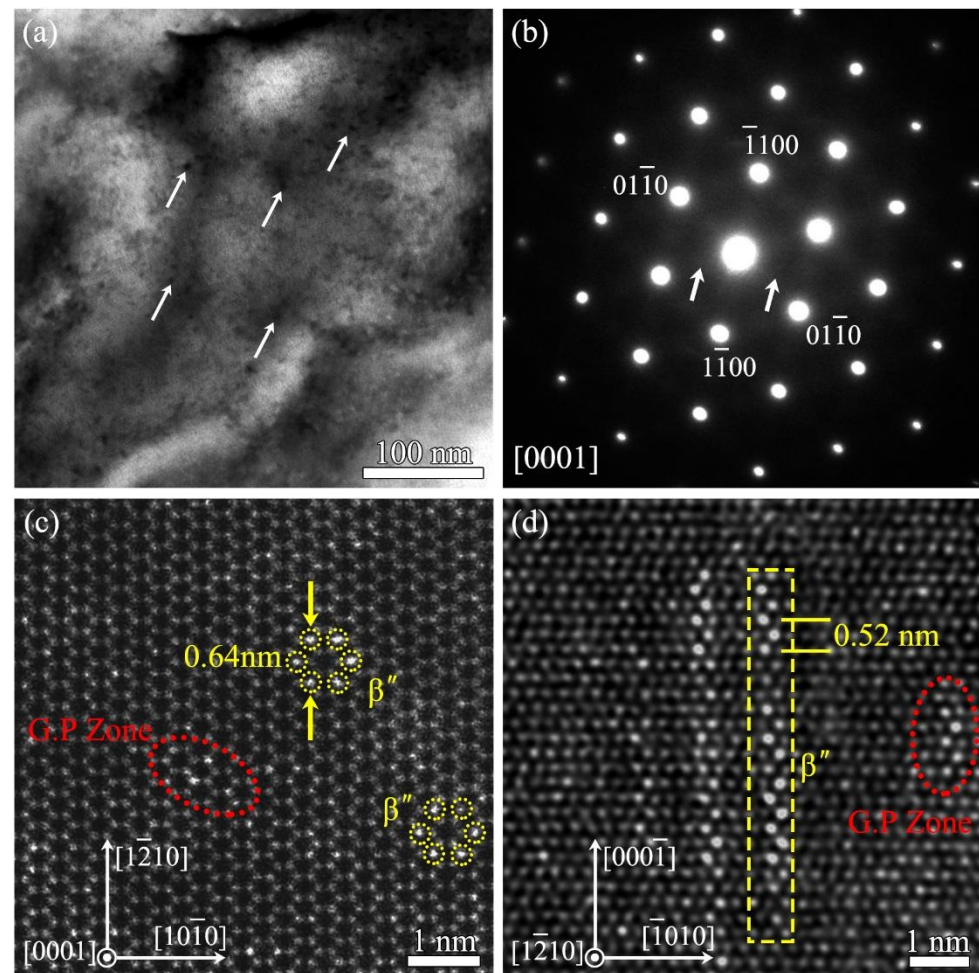


Figure 2. TEM images of Mg-10Gd alloy aged at 200 °C for 0.5 h. (a) Bright field TEM image taken along [0001] zone axis; (b) corresponding selected area diffraction pattern; (c,d) atomic-scaled HAADF-STEM images from [0001] and [1210] zone axis, respectively.

As shown in Figure 2c,d, due to a much higher Z contrast of Gd, the brighter spots represent those of Gd-enriched columns. The G.P. zone and β'' phase are marked by red circles and yellow arrows, respectively. It is clear that the G.P. zone shows higher contrast than the surrounding matrix, though is not a strict periodic structure. It is reasonable to propose the G.P. zone as a precursor of precipitations, which has also been found in other metallic materials [42]. In the earliest stage of aging, we observe some β'' phase formed in the adjacent areas of G.P. zone. The typical structure of β'' phase viewing from [0001] zone axis is a hexagon with six Gd enriched atomic columns at the apexes, as marked by the yellow dotted circles in Figure 2c. The β'' phase has a $D0_{19}$ crystal structure (hexagon, $a = 0.640$ nm and $c = 0.520$ nm) [43]. The morphology of β'' phase is a thin column, with the major axis parallel to c -axis of Mg matrix view from [1210] zone axis. According to atomic-scaled microstructure analysis, the stoichiometric composition of β'' phase is

Mg_3Gd , and the orientation relationship of β'' phase and matrix is $[0001]_{\beta''} // [0001]_{\alpha}$, $(1\bar{2}10)_{\beta''} // (1\bar{2}10)_{\alpha}$.

Figure 3 shows the HAADF-STEM images of the peak aged sample. It is found that high density of β' phase dispersed in grain interior. The morphology from $[0001]$ zone axis is an elliptic shape, which shows a size of ~ 50 nm in length and ~ 10 nm in width (Figure 3a). As shown in Figure 3b, the average thickness of β' phase along c-axis is ~ 100 nm (Figure 3b). Consequently, the three-dimensional structure of β' phase is an elliptic cylinder. The morphology of β' phase has sufficiently high effect on blocking the slip of $\langle a \rangle$ dislocations that is dominated in plastic deformation at room temperature. Figure 3c shows the atomic structure of β' phase, the Gd- and Mg-enriched columns are marked by orange and blue spheres, respectively. Clearly, the minimum period structure from $[0001]$ zone axis is no longer the hexagon marked by the yellow dotted circles in Figure 2c. The β' phase is a coherent precipitate that all the Gd atoms occupy the positions of original Mg atoms. The minimum period structure is a rectangle with length and width of 2.25 nm and 0.66 nm, respectively. Figure 3c shows that ordered substitution of Gd atoms increases the spacing of $\{10\bar{1}0\}$ planes to four times of the origin Mg matrix, which introduces three super lattice spots in the SADP, inserted in Figure 3b. Based on the above experimental results, a three-dimensional unit cell of β' phase is established in Figure 3c. The structure of β' phase is b.c.o structure with lattice parameters of $a = 0.66$ nm, $b = 2.25$ nm and $c = 0.52$ nm. According to the unit cell, its composition is confirmed as Mg_7Gd . Thus, the concentration of Gd element increases significantly during the transformation from β'' phase to β' phase.

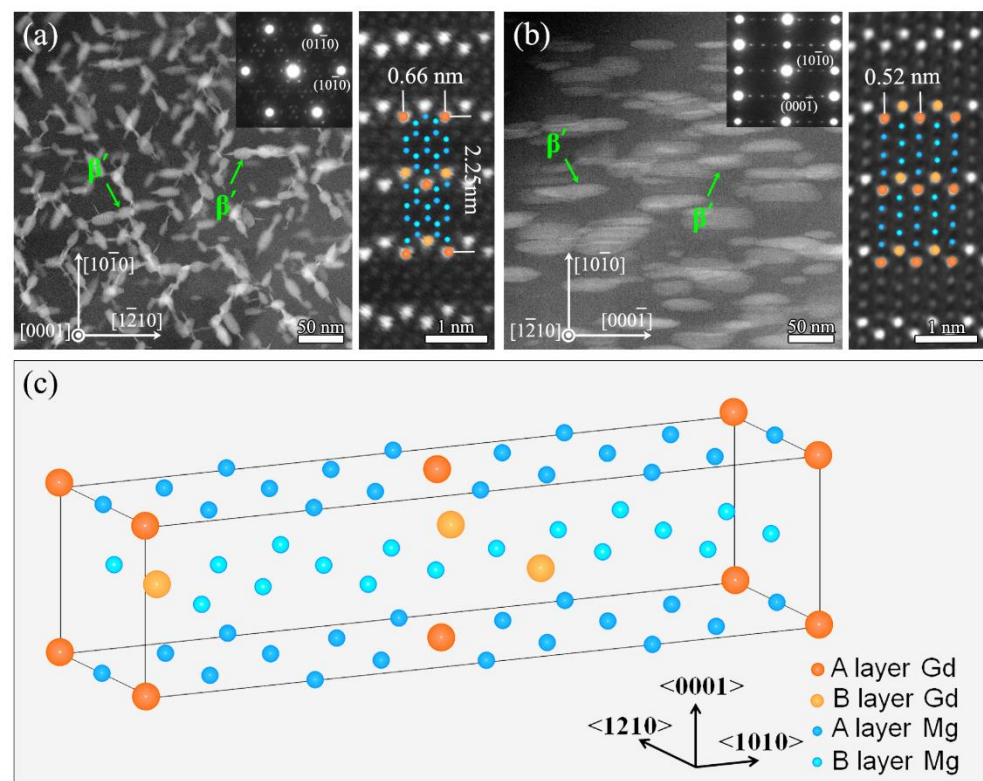


Figure 3. Microstructure of β' phase in the Mg-10Gd alloy aged at 200 °C for 70 h. (a) HAADF-STEM image in $[0001]$ zone axis; (b) HAADF-STEM image in $[1\bar{2}10]$ zone axis; (c) three-dimensional atomic model of the unit cell of β' phase.

Figure 4 shows the microstructure of over aged Mg-10Gd alloy. All the micrographs are taken from $[0001]$ zone axis. After aging treatment for 200 h, the dominated precipitate still is β' phase. However, the length of β' phase is increased to more than 100 nm. The β' phases, similar to connected chains, divides the grain to lots of cells with a diameter of ~ 50 nm.

Figure 4b shows a close-up HAADF-STEM image. Interestingly, the microstructures at the necking parts between main bodies of β' phases are different, as marked by the white arrows. Two typical morphologies with “zig-zag” and “hexagon” shapes, respectively, are observed. As shown in Figure 4c, the metastable phase with zig-zag shape between β' phase is β_T phase. The β_T phase has an orthorhombic crystal structure with lattice parameters of $a = 0.64$ nm, $b = 3.33$ nm and $c = 0.52$ nm, with a composition of Mg_5Gd [24]. In contrast, another metastable phase, with six brighter spots at the apex of a hexagon, is also found, as shown in Figure 4d. This metastable phase is proposed as β_M phase in Ref [44]. Both the β_T and β_M phases are metastable, forming during the transition of β' phase to β_1 phase. Owing to the increasing of spacing between the precipitates, the strength of the over-aged sample is decreased.

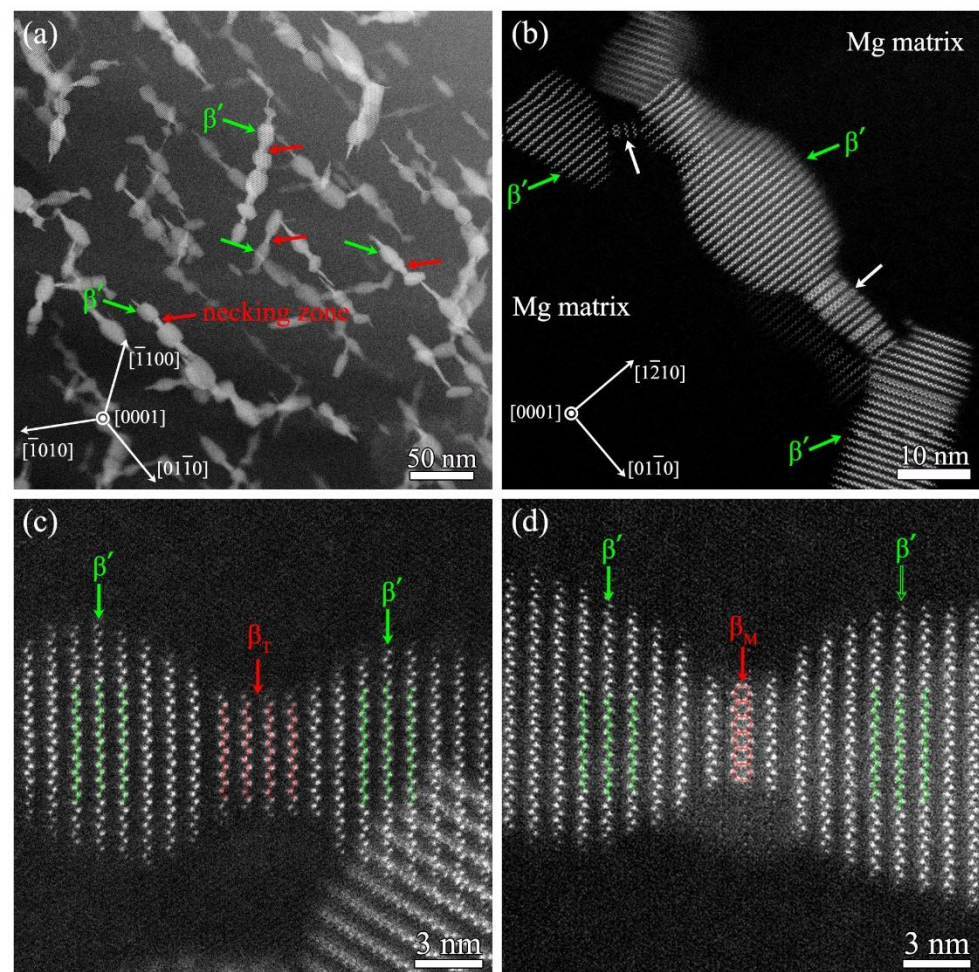


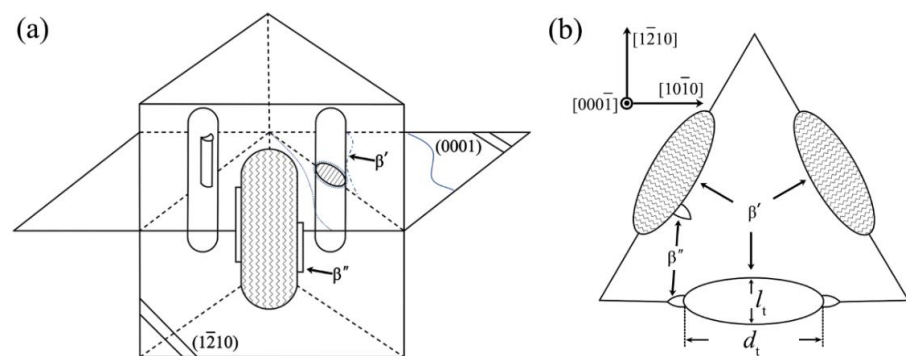
Figure 4. HAADF-STEM images of the Mg-10Gd alloy aged at 200 °C for 200 h. (a,b) low magnification image in [0001] zone axis; (c,d) atomic microstructure show two β' phases connected by β_T and β_M phases, respectively.

To clarify the evolution of β' phase, we statistically analyzed the changing of precipitate size during aging treatment. As listed in Table 1, a clearly nucleation and growth of β' phase is occurred during the period from 10–30 h. However, the growing speed decreases significantly after 30 h. During the period from 30–70 h, the density of β' phase is increased significantly, resulting in rapid increasement of the hardness. During the over aged period (from 70 to 200 h), the length and width of β' phase stays stable, while the thickness along the c -axis exhibits a slight increase from 45 to 48 nm.

Table 1. The size of β' phases in Mg-10Gd alloy with different states.

Aging Time	Size Along Short Axis (d_t , nm)	Size Along Long Axis (l_t , nm)	Size Along $\langle 0001 \rangle$ Direction (nm)
10 h	5.3	5.81	12.83
30 h	11.46	7.58	28.18
50 h	13.72	8.1	31.83
70 h	16.97	9.1	45.69
200 h	16.64	10.68	48.8

It is well studied that the mechanism of plastic deformation of Mg alloys is dominated by basal slip. As shown in Figure 5a, the section of basal planes and precipitates is critical for the blocking effect of dislocation slips. In other words, the $\langle a \rangle$ dislocations with Burger's vector of $\langle 1\bar{2}10 \rangle$ will be blocked by the elliptic barriers. As illustrated in Figure 5b, the β' phase has a larger area than those of the β'' , β_T and β_M phases. Nie et al. reported that a higher strengthening of precipitates is related to two factors. One is the larger effective diameter of the precipitation sections, while the other is the higher density of precipitates [39]. According to the Orowan mechanism, the elliptic cylinder β' phase provides significant pinning effect on the basal slips.

**Figure 5.** Schematic diagram of the interaction between β' phase morphology and $\langle a \rangle$ dislocations. (a) pinning effect of β' phase to basal slip; (b) projection of β' phases on a (0001) plane.

4. Conclusions

In this work, a systematic analysis on evolution of precipitations and corresponding effect on mechanical properties are investigated. The Orowan mechanism is proposed as the main strengthening mechanism in the aged Mg-10Gd alloy. The key findings are summarized as follows:

1. Significant improvement of mechanical properties is achieved by aging treatment, which has a linear correlation with hardness. An optimized aging treatment that perform at 200 °C for 70 h improves the hardness to 120 HV from the initial 72 HV, and the UTS is increased from 170 MPa to 300 MPa;
2. Most precipitations nucleated at early stage of aging treatment are G.P. Zone and β'' phases. The morphology of β'' phase is a thin column, with a $D0_{19}$ crystal structure (hexagon, $a = 0.640$ nm and $c = 0.520$ nm). The orientation relationship of β'' phase and matrix is $[0001]_{\beta''} // [0001]_{\alpha}$, $(1\bar{2}10)_{\beta''} // (1\bar{2}10)_{\alpha}$;
3. At the stage of peak aging, a high density of β' phase is formed and dispersed in grain interior. The three-dimensional structure of β' phase is an elliptic cylinder. The structure of β' phase is base-centered orthorhombic (b.c.o) with lattice parameters of $a = 0.66$ nm, $b = 2.25$ nm and $c = 0.52$ nm. According to the unit cell, its composition is confirmed as Mg_7Gd ;
4. The enhanced strength of Mg-10Gd alloy is mainly attributed to the type of precipitations and their densities. It is found that nucleation of precipitation occurs with only 0.5 h of aging. Owing to the continuously increasing growth of the β' phase

during 10–70 h of aging, the strength is enhanced significantly, though this comes at the expense of ductility. The phase transformation of β' phase occurs at the over-aging stage, which transforms into the intermediate transition phases, including β_T and β_M phases, leading to a slight decrease of strength.

Author Contributions: Conceptualization, H.Z. and L.X.; methodology, B.G. and X.S.; validation, Y.L., Y.S. and N.L.; investigation, Y.L., Y.S. and N.L.; data curation, Y.L., Y.S. and N.L.; writing—original draft preparation, Y.L. and H.Z.; writing—review and editing, L.X. and H.Z.; TEM visualization, M.X. and B.C.; funding acquisition, B.G., L.X. and H.Z. All authors have read and agreed to the published version of the manuscript.

Funding: This work was supported by the National Key R&D Program of China (grant number 2021YFA1200203), the Key Program of National Natural Science Foundation of China (grant number 51931003), the National Natural Science Foundation of China (grant numbers 52071178, 52171118 and 51901103), the Projects in Science and Technique Plans of Ningbo City (No. 2019B10083), the Natural Science Foundation of Jiangsu Province (grant number BK20211197), the China Postdoctoral Science Foundation (grant number 2021M701715).

Institutional Review Board Statement: Not applicable.

Informed Consent Statement: Not applicable.

Data Availability Statement: Not applicable.

Acknowledgments: We also thank the technical support from the Jiangsu Key Laboratory of Advanced Micro&Nano Materials and Technology. The SEM and TEM experiments are performed at the Materials Characterization and Research Center of Nanjing University of Science and Technology.

Conflicts of Interest: The authors declare no conflict of interest.

References

- Joost, W.J.; Krajewski, P.E. Towards magnesium alloys for high-volume automotive applications. *Scripta Mater.* **2017**, *128*, 107–112. [[CrossRef](#)]
- Kiani, M.; Gandikota, I.; Rais-Rohani, M.; Motoyama, K. Design of lightweight magnesium car body structure under crash and vibration constraints. *J. Magnes. Alloy.* **2014**, *2*, 99–108. [[CrossRef](#)]
- Yang, Y.; Xiong, X.; Chen, J.; Peng, X.; Chen, D.; Pan, F. Research advances in magnesium and magnesium alloys worldwide in 2020. *J. Magnes. Alloy.* **2021**, *9*, 705–747. [[CrossRef](#)]
- Pan, H.C.; Xie, D.S.; Li, J.R.; Xie, H.B.; Huang, Q.Y.; Yang, Q.S.; Qin, G.W. Development of novel lightweight and cost-effective Mg-Ce-Al wrought alloy with high strength. *Mater. Res. Lett.* **2021**, *9*, 329–335. [[CrossRef](#)]
- Wei, K.; Xiao, L.R.; Gao, B.; Li, L.; Liu, Y.; Ding, Z.G.; Liu, W.; Zhou, H.; Zhao, Y.H. Enhancing the strain hardening and ductility of Mg-Y alloy by introducing stacking faults. *J. Magnes. Alloy.* **2020**, *8*, 1221–1227. [[CrossRef](#)]
- Wei, K.; Hu, R.; Yin, D.D.; Xiao, L.R.; Pang, S.; Cao, Y.; Zhou, H.; Zhao, Y.H.; Zhu, Y.T. Grain size effect on tensile properties and slip systems of pure magnesium. *Acta Mater.* **2021**, *206*, 116604. [[CrossRef](#)]
- Lu, J.W.; Yin, D.D.; Huang, G.H.; Quan, G.F.; Zeng, Y.; Zhou, H.; Wang, Q.D. Plastic anisotropy and deformation behavior of extruded Mg-Y sheets at elevated temperatures. *Mater. Sci. Eng. A* **2017**, *700*, 598–608. [[CrossRef](#)]
- Yin, D.D.; Boehlert, C.J.; Long, L.J.; Huang, G.H.; Zhou, H.; Zheng, J.; Wang, Q.D. Tension-compression asymmetry and the underlying slip/twinning activity in extruded Mg-Y sheets. *Int. J. Plast.* **2021**, *136*, 102878. [[CrossRef](#)]
- Ma, L.N.; Xie, K.; Cai, J.; Hemker, K.J. Non-dissociated $\langle c+a \rangle$ dislocations in an AZ31 alloy revealed by transmission electron microscopy. *Mater. Res. Lett.* **2020**, *81*, 45–150. [[CrossRef](#)]
- Guo, W.; Wang, Q.D.; Ye, B.; Li, X.C.; Liu, X.T.; Zhou, H. Microstructural refinement and homogenization of Mg-SiC nanocomposites by cyclic extrusion compression. *Mater. Sci. Eng. A* **2012**, *556*, 267–270. [[CrossRef](#)]
- Zhou, H.; Ning, H.Y.; Ma, X.L.; Yin, D.D.; Xiao, L.R.; Sha, X.C.; Yu, Y.D.; Wang, Q.D.; Li, Y.S. Microstructural evolution and mechanical properties of Mg-9.8Gd-2.7Y-0.4Zr alloy produced by repetitive upsetting. *J. Mater. Sci. Technol.* **2018**, *34*, 1067–1075. [[CrossRef](#)]
- Huang, G.H.; Yin, D.D.; Lu, J.W.; Zhou, H.; Zeng, Y.; Quan, G.F.; Wang, Q.D. Microstructure, texture and mechanical properties evolution of extruded fine-grained Mg-Y sheets during annealing. *Mater. Sci. Eng. A* **2018**, *720*, 24–35. [[CrossRef](#)]
- Zhang, L.; Ye, B.; Liao, W.J.; Zhou, H.; Guo, W.; Wang, Q.D.; Jiang, H.Y.; Ding, W.J. Microstructure evolution and mechanical properties of AZ91D magnesium alloy processed by repetitive upsetting. *Mater. Sci. Eng. A* **2015**, *641*, 62–70. [[CrossRef](#)]
- Yang, Y.; Chen, X.; Nie, J.F.; Wei, K.; Mao, Q.Z.; Lu, F.H.; Zhao, Y.H. Achieving ultra-strong Magnesium-lithium alloys by low-strain rotary swaging. *Mater. Res. Lett.* **2021**, *9*, 255–262. [[CrossRef](#)]
- Guo, W.; Wang, Q.D.; Liu, M.P.; Peng, T.; Liu, X.T.; Zhou, H. Microstructure and mechanical performance of AZ31-1.7 wt.% Si alloy processed by cyclic channel die compression. *Mater. Sci. Forum* **2010**, *667–669*, 457–461. [[CrossRef](#)]

16. Guo, W.; Wang, Q.D.; Li, W.Z.; Zhou, H.; Zhang, L.; Liao, W.J. Enhanced microstructure homogeneity and mechanical properties of AZ91-SiC nanocomposites by cyclic closed-die forging. *J. Compos. Mater.* **2016**, *51*, 681–686. [[CrossRef](#)]
17. Qiu, D.; Zhao, P.Y.; Trinkle, D.R.; Wang, Y.Z. Stress-dependent dislocation core structures leading to non-Schmid behavior. *Mater. Res. Lett.* **2021**, *9*, 134–140. [[CrossRef](#)]
18. Xiao, L.R.; Cao, Y.; Li, S.; Zhou, H.; Ma, X.L.; Mao, L.; Sha, X.C.; Wang, Q.D.; Zhu, Y.T.; Han, X.D. The formation mechanism of a novel interfacial phase with high thermal stability in a Mg-Gd-Y-Ag-Zr alloy. *Acta Mater.* **2019**, *162*, 214–225. [[CrossRef](#)]
19. Ni, R.; Ma, S.J.; Long, L.J.; Zheng, J.; Zhou, H.; Wang, Q.D.; Yin, D.D. Effects of precipitate on the slip activity and plastic heterogeneity of Mg-11Y-5Gd-2Zn-0.5Zr (wt. %) during room temperature compression. *Mater. Sci. Eng. A* **2021**, *804*, 140738. [[CrossRef](#)]
20. Li, Z.H.; Sasaki, T.T.; Shiroyama, T.; Miura, A.; Uchida, K.; Hono, K. Simultaneous achievement of high thermal conductivity, high strength and formability in Mg-Zn-Ca-Zr sheet alloy. *Mater. Res. Lett.* **2020**, *8*, 335–340. [[CrossRef](#)]
21. Wu, G.H.; Jafari Nodooshan, H.R.; Zeng, X.Q.; Liu, W.C.; Li, D.J.; Ding, W.J. Microstructure and High Temperature Tensile Properties of Mg-10Gd-5Y-0.5Zr Alloy after Thermo-Mechanical Processing. *Metals* **2018**, *8*, 980. [[CrossRef](#)]
22. Xue, Z.Y.; Han, X.Z.; Zhou, Z.Y.; Wang, Y.L.; Li, X.S.; Wu, J.P. Effects of Microstructure and Texture Evolution on Strength Improvement of an Extruded Mg-10Gd-2Y-0.5Zn-0.3Zr Alloy. *Metals* **2018**, *8*, 1087. [[CrossRef](#)]
23. Zhang, J.H.; Liu, S.J.; Wu, R.Z.; Hou, L.; Zhang, M.L. Recent developments in high-strength Mg-RE-based alloys: Focusing on Mg-Gd and Mg-Y systems. *J. Magnes. Alloy.* **2018**, *6*, 277–291. [[CrossRef](#)]
24. Zhou, H.; Xu, W.Z.; Jian, W.W.; Cheng, G.M.; Ma, X.L.; Guo, W.; Mathaudhu, N.S.; Wang, Q.D.; Zhu, Y.T. A new metastable precipitate phase in Mg-Gd-Y-Zr alloy. *Philos. Mag.* **2014**, *94*, 2403–2409. [[CrossRef](#)]
25. Panigrahi, S.K.; Mishara, R.S.; Brennan, R.C.; Cho, K. Achieving extraordinary structural efficiency in a wrought magnesium rare earth alloy. *Mater. Res. Lett.* **2020**, *8*, 151–157. [[CrossRef](#)]
26. Xiao, L.R.; Chen, X.F.; Ning, H.Y.; Jiang, P.; Liu, Y.; Chen, B.; Yin, D.D.; Zhou, H.; Zhu, Y.T. Unexpected high-temperature brittleness of a Mg-Gd-Y-Ag alloy. *J. Magnes. Alloy.* **2021**, in press. [[CrossRef](#)]
27. Jafari Nodooshan, H.R.; Wu, G.H.; Liu, W.C.; Wei, G.L.; Li, Y.L.; Zhang, S. Effect of Gd content on high temperature mechanical properties of Mg-Gd-Y-Zr alloy. *Mater. Sci. Eng. A* **2016**, *651*, 840–847. [[CrossRef](#)]
28. Su, N.; Wu, Y.J.; Deng, Q.; Chang, Z.; Wu, Q.; Xue, Y.; Yang, K.; Chen, Q.; Peng, L. Synergic effects of Gd and Y contents on the age-hardening response and elevated-temperature mechanical properties of extruded Mg-Gd(-Y)-Zn-Mn alloys. *Mater. Sci. Eng. A* **2021**, *810*, 141019. [[CrossRef](#)]
29. Mo, N.; McCarroll, I.; Tan, Q.; Ceguerra, A.; Liu, Y.; Cairney, J.; Dieringa, H.; Huang, Y.; Jiang, B.; Pan, F.; et al. Understanding solid solution strengthening at elevated temperatures in a creep-resistant Mg-Gd-Ca alloy. *Acta Mater.* **2019**, *181*, 185–199. [[CrossRef](#)]
30. Ashrafizadeh, S.M.; Mahmudi, R. Effects of Gd, Y, and La Rare-Earth Elements on the Microstructural Stability and Elevated-Temperature Mechanical Properties of AZ81 Magnesium Alloy. *Metall. Mater. Trans. A* **2019**, *50*, 5957–5968. [[CrossRef](#)]
31. Liu, H.; Huang, H.; Wang, C.; Ju, J.; Sun, J.P.; Wu, Y.N.; Jiang, J.H.; Ma, A.B. Comparative Study of Two Aging Treatments on Microstructure and Mechanical Properties of an Ultra-Fine Grained Mg-10Y-6Gd-1.5Zn-0.5Zr Alloy. *Metals* **2018**, *8*, 658. [[CrossRef](#)]
32. Kandalam, S.; Agrawal, P.; Avadhani, G.S.; Kumar, S.; Suwas, S. Precipitation response of the magnesium alloy WE43 in strained and unstrained conditions. *J. Alloy. Compd.* **2015**, *623*, 317–323. [[CrossRef](#)]
33. Zhang, F.; Wang, Y.F.; Duan, Y.B.; Wang, K.J.; Wang, Y.T.; Zhang, W.J.; Hu, J. Precipitation processes during the peak-aged and over-aged stages in an Mg-Gd-Y-Zr alloy. *J. Alloy. Compd.* **2019**, *788*, 541–548. [[CrossRef](#)]
34. Xu, C.; Zheng, M.Y.; Wu, K.; Wang, E.D.; Fan, G.H.; Xu, S.W.; Kamado, S.; Liu, X.D.; Wang, G.J.; Lv, X.Y. Effect of ageing treatment on the precipitation behaviour of Mg-Gd-Y-Zn-Zr alloy. *J. Alloy. Compd.* **2013**, *550*, 50–56. [[CrossRef](#)]
35. Sha, X.C.; Xiao, L.R.; Chen, X.F.; Cheng, G.M.; Yu, Y.D.; Yin, D.D.; Zhou, H. Atomic structure of γ'' phase in Mg-Gd-Y-Ag alloy induced by Ag addition. *Philos. Mag.* **2019**, *99*, 1957–1969. [[CrossRef](#)]
36. Li, R.G.; Nie, J.F.; Huang, G.J.; Xin, Y.C.; Liu, Q. Development of high-strength magnesium alloys via combined processes of extrusion, rolling and ageing. *Scripta Mater.* **2011**, *64*, 950–953. [[CrossRef](#)]
37. He, S.M.; Zeng, X.Q.; Peng, L.M.; Gao, X.; Nie, J.F.; Ding, W.J. Precipitation in a Mg-10Gd-3Y-0.4Zr (wt.%) alloy during isothermal ageing at 250 °C. *J. Alloy. Compd.* **2006**, *421*, 309–313. [[CrossRef](#)]
38. Nie, J.F. Precipitation and Hardening in Magnesium Alloys. *Metall. Mater. Trans. A* **2021**, *43*, 3891–3939. [[CrossRef](#)]
39. Nie, J.F. Effects of precipitate shape and orientation on dispersion strengthening in magnesium alloys. *Scripta Mater.* **2003**, *48*, 1009–1015. [[CrossRef](#)]
40. Zhang, Q.; Fan, T.W.; Fu, L.; Tang, B.Y.; Peng, L.M.; Ding, W.J. Ab-initio study of the effect of rare-earth elements on the stacking faults of Mg solid solutions. *Intermetallics* **2012**, *29*, 21–26. [[CrossRef](#)]
41. Liu, Z.Q.; Qian, Q.; Jiang, Y.; Wang, Y.R.; Zhu, Y.M.; Nie, J.F. Incoherent tilt grain boundaries stabilized by stacking faults and solute-cluster segregation: A case-study of an Mg-Gd alloy. *Mater. Res. Lett.* **2020**, *8*, 268–274. [[CrossRef](#)]
42. Sun, W.W.; Zhu, Y.M.; Marceau, R.; Wang, L.Y.; Zhang, Q.; Gao, X.; Hutchinson, C. Precipitation strengthening of aluminum alloys by room-temperature cyclic plasticity. *Science* **2019**, *363*, 972–975. [[CrossRef](#)] [[PubMed](#)]
43. Antion, C.; Donnadieu, P.; Perrard, F.; Deschamps, A.; Tassin, C.; Pisch, A. Hardening precipitation in a Mg-4Y-3RE alloy. *Acta Mater.* **2003**, *51*, 5335–5348. [[CrossRef](#)]
44. Zheng, J.X.; Li, Z.; Tan, L.D.; Xu, X.S.; Luo, R.C.; Chen, B. Precipitation in Mg-Gd-Y-Zr Alloy: Atomic-scale insights into structures and transformations. *Mater. Charact.* **2016**, *117*, 76–83. [[CrossRef](#)]